

High-speed antiferromagnetic domain walls driven by coherent spin waves

Received: 26 June 2025

Accepted: 26 September 2025

Published online: 07 November 2025

 Check for updatesKyle L. Seyler ^{1,2,3}, Hantao Zhang ⁴, Daniel Van Beveren^{1,2}, Costel R. Rotundu ⁵, Young S. Lee ^{5,6}, Ran Cheng ^{4,7} & David Hsieh ^{1,2} ✉

The ability to rapidly manipulate domain walls in magnetic materials is key to developing novel high-speed spintronic memory and computing devices. Antiferromagnetic materials present a particularly promising platform due to their robustness against stray fields and their potential for exceptional domain wall velocities. Among various proposed driving mechanisms, coherent spin waves could potentially propel antiferromagnetic domain walls to the magnon group velocity while minimizing dissipation from Joule heating. However, experimental realization has remained elusive due to the dual challenges of generating coherent antiferromagnetic spin waves near isolated mobile antiferromagnetic domain walls and simultaneously measuring high-speed domain wall dynamics. Here we experimentally realize an approach where ultrafast laser pulses generate coherent spin waves that drive antiferromagnetic domain walls and develop a technique to directly map the spatiotemporal domain wall dynamics. Using the room-temperature antiferromagnetic insulator $\text{Sr}_2\text{Cu}_3\text{O}_4\text{Cl}_2$, we observe antiferromagnetic domain wall motion with record-high velocities up to $\sim 50 \text{ km s}^{-1}$. Remarkably, the direction of domain wall propagation is controllable through both the pump laser helicity and the sign of the domain wall winding number. This bidirectional control can be theoretically explained, and numerically reproduced, by the domain wall dynamics induced by coherent spin waves of the in-plane magnon mode—a phenomenon unique to magnets with an easy-plane anisotropy. Our work uncovers a novel domain wall propulsion mechanism that is generalizable to a wide range of antiferromagnetic materials, unlocking new opportunities for ultrafast coherent antiferromagnetic spintronics.

An emerging approach to drive domain wall (DW) motion is by using magnons—the quanta of spin waves. Thermal magnons can give rise to entropic torques in temperature gradients that move DWs towards hotter regions^{1–7}, a phenomenon widely observed in different magnetic materials^{8–14}. In contrast, our understanding of DWs driven by nonthermal magnons remains limited.

Theories predict that propagating magnons can drive DW motion through the transfer of spin angular momentum or linear momentum upon transmission or reflection^{15–26}. In ferromagnetic systems, experimental evidence for magnonic spin-transfer torque includes the de-pinning of DWs in permalloy using spin wave bursts from colliding DWs²⁷, light-induced magnetoelastic waves shifting DWs in iron

¹Department of Physics, California Institute of Technology, Pasadena, CA, USA. ²Institute for Quantum Information and Matter, California Institute of Technology, Pasadena, CA, USA. ³Wyant College of Optical Sciences, University of Arizona, Tucson, AZ, USA. ⁴Department of Electrical and Computer Engineering, University of California Riverside, Riverside, CA, USA. ⁵Stanford Institute for Materials and Energy Sciences, SLAC National Accelerator Laboratory, 2575 Sand Hill Road, Menlo Park, CA, USA. ⁶Department of Applied Physics, Stanford University, Stanford, CA, USA. ⁷Department of Physics and Astronomy, University of California Riverside, Riverside, CA, USA. ✉e-mail: dhsieh@caltech.edu

garnets²⁸, and coherent magnons from microwave antennas driving DWs in metallic multilayers and iron garnet films at velocities of 10 to ~ 100 m s⁻¹^{29,30}. Beyond ferromagnets, antiferromagnets exhibit complex spin texture dynamics³¹, diverse magnon excitations³², and high DW velocities^{33,34}, which may lead to powerful new approaches for fast DW manipulation^{18,19,21,22,24,35}. However, nonthermal magnonic manipulation of antiferromagnetic (AFM) DWs remains experimentally unrealized.

Ultrafast laser pulses are a versatile way to generate nonthermal magnons in antiferromagnets. It is possible to induce intense coherent AFM spin waves with ultrafast laser light through inverse magneto-optical processes^{36–40}, thermal effects⁴¹, terahertz electromagnetic excitation⁴², and strong absorption⁴³. However, studying the interaction between coherent spin waves and AFM DWs presents three key challenges. First, creating and detecting DWs in antiferromagnets is often more challenging than in ferrimagnets and ferromagnets due to the absence of a net moment⁴⁴. Second, no experiment has mapped the spatiotemporal evolution of light-driven DW motion, which would allow the direct measurement of fast dynamics. Ultrafast stroboscopic pump-probe experiments require the sample to return to its initial state after excitation, complicating the visualization of irreversible DW dynamics⁴⁵. Most studies of light-driven DWs either examine static before-and-after domain structure images without probing the transient behavior¹² or infer spatially averaged dynamics through time-resolved diffraction experiments⁴⁶. Third, ultrafast optical excitation can affect AFM DWs through more trivial thermal effects^{12–14} or non-thermal photoinduced magnetic anisotropy^{47,48}, which must be distinguished from coherent magnonic effects.

Here we overcome these challenges and directly capture the ultrafast-light-induced motion of an AFM DW. Our material of choice, the square-lattice Mott insulator Sr₂Cu₃O₄Cl₂, hosts in-plane Cu spins with strong AFM exchange interactions similar to high-temperature cuprate superconductor parent compounds, where the Cu_l sublattice has $J_1 \approx 130$ meV with a Néel temperature of $T_{N,l} \approx 380$ K (Fig. 1a). However, Sr₂Cu₃O₄Cl₂ is unique in that it contains an additional Cu ion (Cu_{ii}) at the center of every other square plaquette, breaking the equivalence of neighboring Cu_l sites and inducing a weak in-plane ferromagnetic moment **m** locked perpendicular to the Néel vector **n**⁴⁹. Previous work has shown that optical second-harmonic generation (SHG) rotational anisotropy, which is sensitive to magnetic point group symmetries, can detect **m** and **n**, enabling direct visualization of AFM domains and DWs⁵⁰. The locations of the 90° DWs were largely fixed by a built-in spatially dependent uniaxial anisotropy. In ambient field conditions, 180° (antiphase) DWs were not observed, due to poling by the Earth's magnetic field during cooling.

Results and discussion

Creating and characterizing antiphase Néel-type AFM DWs

We first demonstrate controlled creation and positioning of antiphase AFM DWs using applied magnetic fields and laser heating. Polarized wide-field SHG images exhibit distinct bright and dark regions that correspond to magnetic domains with perpendicular **m** orientations (Fig. 1b), as described in ref. 50. Initially, at zero applied magnetic field ($H = 0$), only two domain states are present (**m** along $-x$ and $-y$). By applying H anti-parallel to the $-x$ domain, a third domain state (with **m** along $+x$) becomes more favorable. Eventually, at high-enough H , an antiphase DW would form and propagate through the sample to flip the $-x$ domain to $+x$. To stabilize this antiphase DW within the sample, we fixed H just below this threshold value for antiphase DW formation ($\mu_0 H \approx 6$ G) and scanned the imaging laser across the 90° wall. Local laser heating reduces the coercive field, allowing the formation of an antiphase DW that becomes spatially trapped near the imaging laser center. The antiphase DW manifests as a vertical dark line in the image. Moreover, it can be dragged to different positions by translating the imaging laser (Fig. 1c). The DW prefers the laser center

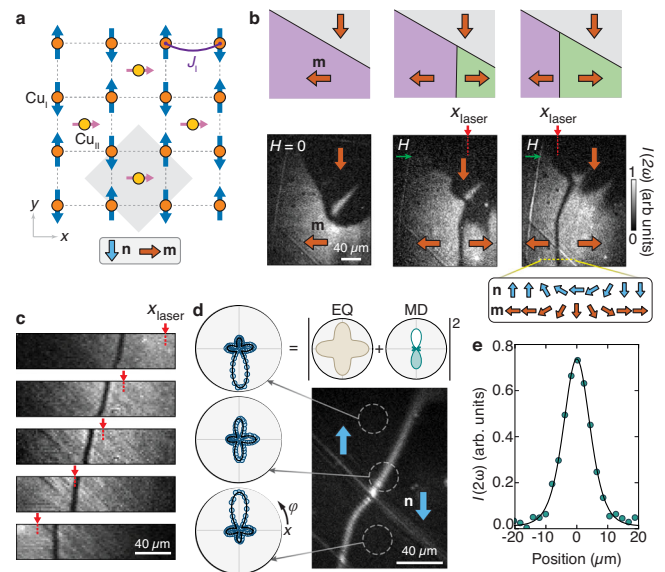


Fig. 1 | Creation and positioning of wide antiphase Néel DWs. **a** Crystal and magnetic structure of the Cu₃O₄ plane of Sr₂Cu₃O₄Cl₂ below $T_{N,l}$. **b** Creation of an antiphase DW at a 90° DW. The bottom row shows SHG images of the process at different applied magnetic field (H) and horizontal laser positions (x_{laser}), while the top row shows a schematic of the domain configuration, labeled by their in-plane moment **m**. The resulting antiphase DW configuration is depicted in the bottom right. The imaging laser is horizontally polarized (along x axis). **c** SHG images of an antiphase DW at different x_{laser} . **d** SHG image of antiphase DW with vertically polarized laser. Rotational anisotropy polar plots of the SHG intensity (for P-polarized input and output electric field polarization measured as a function of the scattering plane angle φ) are shown for selected locations. $\varphi = 0$ corresponds to the x direction. The solid lines are fits to a coherent superposition of crystallographic electric quadrupole (EQ) and AFM-induced magnetic dipole (MD) SHG processes, as described in ref. 50. The EQ and MD processes shown in the figure represent the P_{in} -light-induced nonlinear polarization projected along P_{out} . Filled and unfilled lobes indicate opposite phases. The DW SHG pattern is fit to a three-domain averaged expression, as described in Supplementary Section 1. **e** Line cut of the SHG image intensity perpendicular to an antiphase DW. The solid line shows a fit to the SHG intensity of a DW profile (see Methods) with an extracted DW width $\pi\lambda = 8.98(22)\mu\text{m}$.

due to an entropic torque caused by the laser-induced Gaussian temperature profile.

Next, we characterize the width, type, and winding number of the antiphase DWs. In Fig. 1b and c, the dark DW line could arise from destructive interference of SHG at the boundary of the time-reversed domain states⁵¹. To rule this out, we rotated the imaging laser polarization by 90°, causing the previously bright domain states to appear dark. Surprisingly, the antiphase DW shows comparably bright SHG (Fig. 1d) relative to the single domains in Fig. 1b and c, implying that the DW width must be large compared to the SHG wavelength (400 nm) and that SHG interference between neighboring domains is negligible. A line cut across the DW reveals a DW width $\pi\lambda \approx 9 \mu\text{m}$, where λ is the width parameter, which is larger than both our diffraction limit ($\sim 1 \mu\text{m}$) and the DW widths in typical antiferromagnets such as NiO and Cr₂O₃ (10–100 nm)^{52,53}. The wide antiphase DWs are a consequence of the large J_1 combined with relatively weak in-plane easy-axis anisotropy (K)^{49,54} since the width scales as $\sqrt{J_1/K}$.

The large DW width enables us to determine the orientation of **n** within the DW using scanning SHG rotational anisotropy. In single-domain regions, SHG patterns exhibit a strong lobe oriented along $-\mathbf{n}$, consistent with prior results⁵⁰ (Fig. 1d). In contrast, the DW region shows a pattern characteristic of a superposition of the two single-domain states (Supplementary Section 1). Notably, the $\varphi = 0^\circ$ lobe is more intense than the $\varphi = 180^\circ$ lobe, indicating that **n** is oriented along

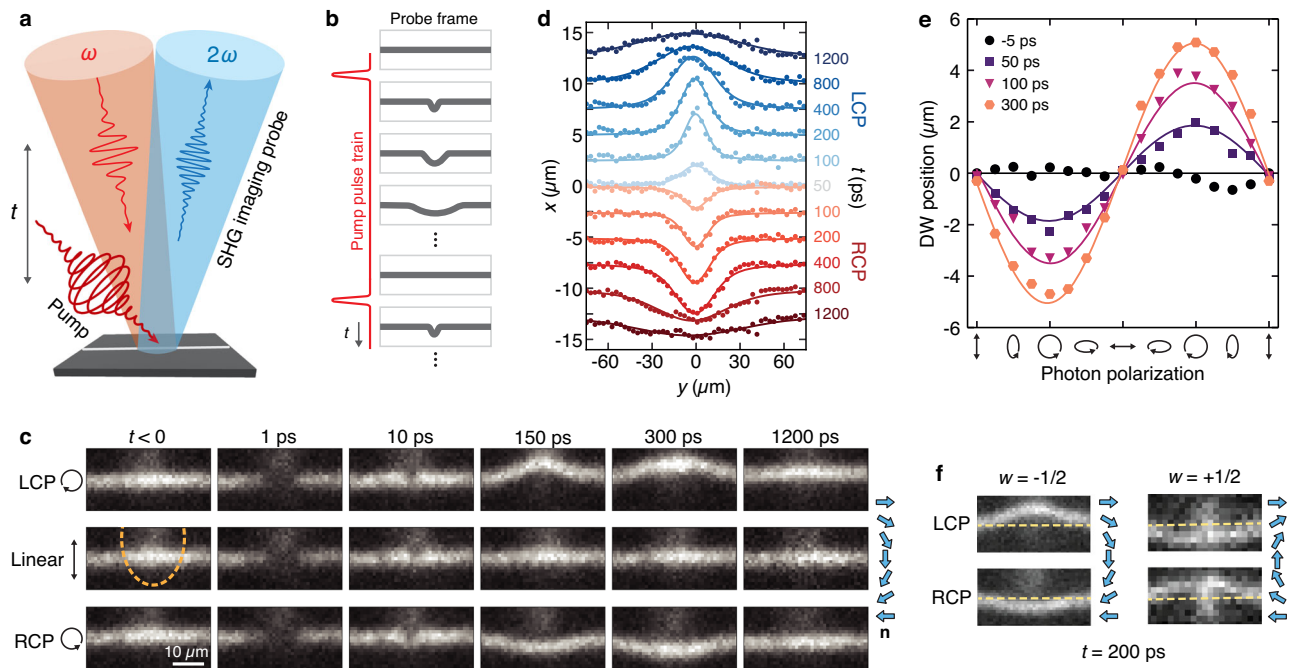


Fig. 2 | Observation of helicity-dependent light-driven DW motion. **a** Schematic of pump-probe SHG imaging experiment. The pump beam is focused obliquely on the sample at -10° angle of incidence, while the SHG imaging probe is near-normal incidence. **b** Schematic of the DW position at different times before and after each pulse of pump excitation train. **c** SHG images of an antiphase DW at selected pump-probe time delays for linear, left circular, and right circular pump polarizations. The dashed oval indicates the pump excitation spot, which is offset from the DW center. The DW configuration is displayed on the right. **d** Extracted dynamics of the DW shape for left and right circular pump. The solid curves are fits to a Voigt profile. The data at different delays are vertically offset for clarity. **e** Pump photon

polarization dependence of the maximum DW position (at $x = 0$) for different time delays. The horizontal axis runs from $\theta = -90^\circ$ to $\theta = 90^\circ$, where θ is the linear polarization angle before entering a quarter-wave plate with fixed fast axis at 0° . The solid curves are fits proportional to $\sin(2\theta)$. **f** SHG images at $t = 200$ ps for different pump photon helicities and DW winding numbers w . The dashed lines indicate the initial DW position at $t < 0$. The additional intensity outside the DW location arises due to scattered SHG from the pump beam as well as a contribution from spin wave precession for $t > 0$ (see main text). The vertical scale of each image is $20 \mu\text{m}$.

$-x$ at the DW center. These results confirm that the DW is Néel-type (Fig. 1b inset), where the spins rotate within the sample plane, perpendicular to the DW normal, as expected from the easy-plane anisotropy of the parent cuprates. We may characterize its anti-clockwise sense of spin rotation through a winding number $w = -1/2$, which gives the number of times the spins wrap around a circle in the clockwise direction ($w = \frac{1}{2\pi} \int_{-\infty}^{+\infty} \partial_x \phi(x) dx$, where $\phi(x)$ is the in-plane Néel vector angle at position x along the wall). Our SHG measurements can therefore fully characterize the width, type, and winding number of the AFM DWs.

Spatiotemporal mapping of helicity-dependent DW dynamics

We now proceed to study the dynamics after ultrafast optical excitation on the AFM DWs using time-resolved pump-probe SHG imaging. Figure 2a illustrates the experimental configuration. We used 100 fs pump pulses (fluence $8 \text{ mJ}/\text{cm}^2$) at 1.55 eV , below the 1.86 eV charge gap⁵⁵, focused at slightly oblique incidence to an elliptical spot on the DW, while time-delayed wide-field SHG imaging pulses served as the probe (see Methods). The laser repetition rate is 100 kHz with SHG imaging integration times of $\sim 10^{-5}$ seconds, so each final image consists of an average of $\sim 10^{10}$ individual pump excitation events. Therefore, in order to resolve the spatiotemporal dynamics, the DW must return to its original state before the next pulse in the train arrives (Fig. 2b). Here we realize reversible DW motion through the combined effects of DW surface tension and the photothermal trapping potential of the large SHG imaging beam (Fig. 1c), which generate restoring forces against localized perturbations. Under either linearly or circularly polarized pumping, the DW SHG intensity strongly decreases soon after time zero ($t = 1 \text{ ps}$). This indicates ultrafast suppression of the 3D long-range AFM order due to photothermal heating, though in-plane short-range

order can still persist⁵⁵. Within 10 ps , the DW almost fully recovers, consistent with previously measured spin dynamics in $\text{Sr}_2\text{Cu}_3\text{O}_4\text{Cl}_2$ ⁵⁵. At later times, we observe no subsequent changes in the SHG images for linearly polarized pumping. In contrast, left or right circularly polarized pump pulses induce striking changes, driving the DW locally up or down, respectively, followed by a slower relaxation back to the equilibrium DW position. The crisp DW images demonstrate that the motion is reversible. We extract the DW shape by fitting to vertical line cuts across the wall and plotting the center positions as shown in Fig. 2d. This illustrates how the DW not only propagates up or down normal to itself but also moves outwards to the left and right, tens of microns beyond the pump laser pulse spot. Interestingly, these complex DW dynamics occur well after the 100 fs pump light has interacted with the sample, as visualized in Supplementary Videos 1 and 2.

Coherent spin waves drive the DW motion

To uncover the origin of the light-induced DW motion, we explored different pump laser parameters and DW configurations. First, we systematically adjusted the pump polarization between linear, elliptical, and circular states, finding maximal DW displacement for circularly polarized light, with opposite helicities driving motion in opposite directions (Fig. 2d). Photoinduced magnetic anisotropy can thus be ruled out, as it should occur under linear but not circular polarization⁵⁶. In addition, the absence of DW displacement in the linear pump case implies that transient photothermal gradients do not drive the motion¹². Further evidence against a heating effect comes from the observation that, for a fixed helicity, the direction of DW motion is independent of whether the pump laser spot is offset to one side or the other of the DW (Supplementary Section 2). One might also propose that an effective in-plane photo-induced magnetic field³⁶

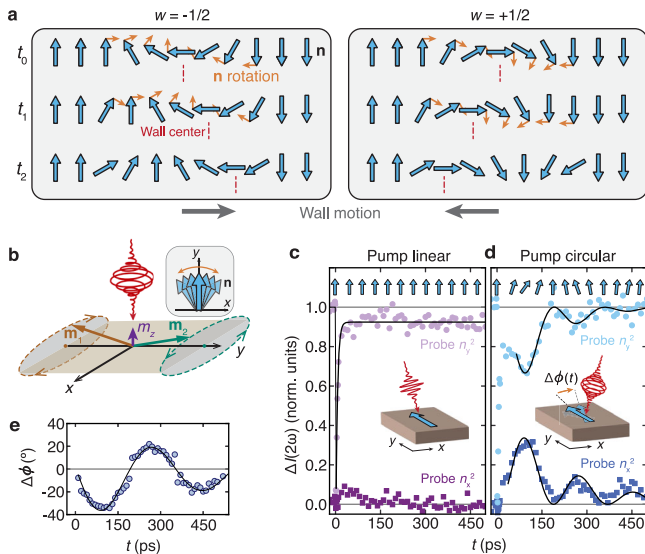


Fig. 3 | Mechanism of light-driven DWs. **a** Schematic of Néel-type DW at different times (t_0 , t_1 , t_2) after clockwise rotations of \mathbf{n} for negative (left panel) and positive (right panel) winding number. **b** Schematic of coherent in-plane magnon induced by a circularly polarized laser pulse. \mathbf{m}_1 and \mathbf{m}_2 indicate the sublattice moments and m_z is the out-of-plane moment induced by laser. The Néel vector $\mathbf{n} = (\mathbf{m}_2 - \mathbf{m}_1)/2$ initially rotates in the clockwise direction and its full trajectory is a back-and-forth oscillation in the xy plane (inset). **c** SHG transients for linear pump excitation with the probe beam linearly polarized in the \hat{x} (circular markers) or \hat{y} (square markers) direction, giving SHG proportional to n_x^2 or n_y^2 respectively. The black curves are guides to the eye. **d** Same as **c** but with circularly polarized pump. The black curves are fitted to the square of a damped sine wave: $I_{\text{SHG}} = I_0(\sin(2\pi ft + \phi_0)e^{-t/\tau})^2$, where I_0 is the intensity, f is the frequency of oscillation, ϕ_0 is a phase offset, and τ is the decay time constant. **e** Extracted change in Néel vector angle, $\Delta\phi(t)$, using the case of circular pump with \hat{x} probe in **d**. Since the SHG cannot distinguish between positive and negative $\Delta\phi$, we have chosen the signs of the data to give agreement with $f \approx 2.8$ GHz found in **d**. The black curve is a fit to a damped sine wave.

generated from an oblique incidence circularly polarized pump laser could move the DW by coupling to its weak in-plane ferromagnetism, but we found no dependence on the pump scattering plane angle (Supplementary Section 3). Next, we examined how the DW configuration influences its motion. By starting with different initial 90° DW states (Fig. 1b), we could prepare other antiphase DW configurations that possess time-reversed DW spins or opposite sign of w (i.e., whether the spins rotate clockwise or anti-clockwise). We observed that changing the sign of w reversed the DW direction for a fixed pump helicity, as shown in Fig. 2f. On the other hand, when the winding number was fixed, time-reversing the DW state (i.e., flipping each spin) did not affect its motion (Supplementary Section 4). These results establish that the direction of DW motion is determined by a combination of the DW winding number sign and pump helicity.

This unique dependence on pump helicity and wall winding suggests an intuitive picture for the initiation of DW motion. Consider a Néel wall in an easy-plane antiferromagnet, where \mathbf{n} can either rotate clockwise or anti-clockwise within the two-dimensional plane as one moves from left to right across the wall (Fig. 3a). If there is a local clockwise rotation of \mathbf{n} within the DW, the wall center position will move to the left (right) for positive (negative) winding number, while anti-clockwise rotation of \mathbf{n} produces the opposite motion. Ultrafast laser pulses can induce such a rotation of \mathbf{n} through the excitation of coherent spin waves (the in-plane mode)³⁷. Circularly polarized light normally incident upon the sample injects spin angular momentum along $\pm\hat{z}$, with the sign determined by the helicity. This angular momentum cants the Cu_1 sublattice moments (\mathbf{m}_1 and \mathbf{m}_2) toward the $\pm z$ direction, causing an instantaneous non-collinearity between \mathbf{m}_1

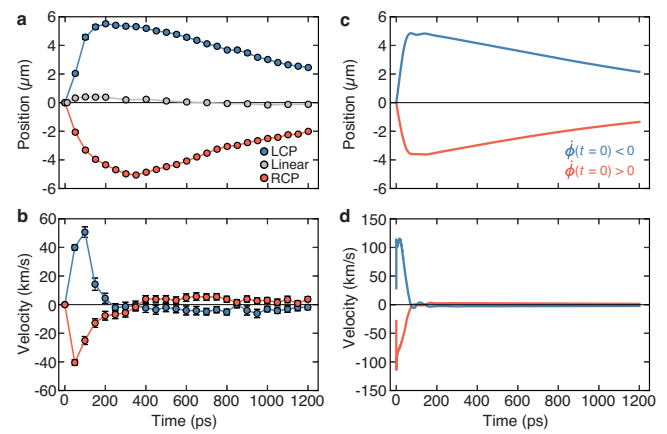


Fig. 4 | Quantitative extraction of DW dynamics and comparison to simulation. **a, b** Position (**a**) and velocity (**b**) of the DW center (at the location of maximum displacement) over time for different pump polarizations. Error bars represent one standard error for the fitted DW positions and the corresponding propagated error for calculated velocities. **c, d** Simulated time dependence of the DW position (**c**) and velocity (**d**) for positive and negative initial angular velocities of the Néel vector.

and \mathbf{m}_2 , which generates an in-plane (xy) rotation of \mathbf{n} through the exchange interaction (Fig. 3b)⁵⁷. Consequently, the pump helicity sets the initial rotation direction of \mathbf{n} , thereby setting the initial DW motion. An effective view is that the photon spin angular momentum is transferred to the DW and drives its motion, forming a spin current. As \mathbf{n} reverses directions, a slowdown and a reversal of the wall direction occurs. Notably, we observe no oscillations in the DW position. This is likely due to the strong damping of \mathbf{n} oscillations, particularly near the DW where energy is transferred to the wall motion.

To search for evidence of light-induced coherent AFM spin waves, we performed time-resolved SHG intensity measurements on a single magnetic domain region. The desired magnon mode corresponds to \mathbf{n} oscillations in the xy plane, characterized by an exchange of intensity between its x and y components (n_x and n_y). Normal incidence SHG intensity for linearly polarized excitation along \hat{x} (\hat{y}) is proportional to n_x^2 (n_y^2), allowing us to measure light-induced rotational changes of \mathbf{n} . Figure 3c shows the normalized change in SHG intensity after linearly polarized pumping on a domain with $\mathbf{n} = n_y\hat{y}$. As expected, n_y is suppressed on ultrafast timescales and recovers within ~ 10 ps, while n_x shows no appreciable changes. In contrast, for the same scenario under circularly polarized excitation (Fig. 3d), \mathbf{n} oscillates in the plane at ~ 2.8 GHz, corresponding to the low-frequency in-plane magnon mode depicted in Fig. 3b that has previously been measured by electron spin resonance⁵⁸. Using the SHG data in Fig. 3d, and assuming $\phi(t=0) < 0$, we can reconstruct the trajectory of \mathbf{n} and find a maximum initial rotation angle of $\sim 33^\circ$ (Fig. 3e). Since the excited spin waves are quasi-uniform (optical pump spot size $\sim 30 \mu\text{m}$), no appreciable spin wave propagation outside the pumped region is observed. Even though the Néel vector is initially suppressed by the pump, coherent magnons can still be launched due to the presence of in-plane magnetic correlations.

Quantitative analysis of high-speed DW motion and comparison to simulations

To quantify the light-driven DW motion, we analyzed its position and velocity over time at the location of maximum DW displacement ($x = 0$ in Fig. 2d). Figure 4a, b shows the temporal evolution of the wall center position (velocity) for different pump helicities. The DW position rapidly shifts in the first ~ 100 ps with a maximum velocity of $\sim 50 \text{ km s}^{-1}$ (Fig. 4b), slows down from 100 ps to 200 ps reaching a maximum displacement of $\sim 6 \mu\text{m}$, and then reverses direction back to

equilibrium at -5 km s^{-1} . The $\sim 100 \text{ ps}$ timescale of the fast outward wall motion is similar to the timescale of the initial \mathbf{n} rotation identified in Fig. 3e. Furthermore, reducing the pump fluence does not appreciably change this timescale (Supplementary Section 5), although it decreases the maximum velocity and position. These observations confirm the causal chain: the ultrafast optical pulse rapidly excites coherent spin waves, which subsequently propel the DW over a significantly longer timescale. The slight asymmetry between left and right circularly polarized cases is likely due to the small spatial offset between pump laser spot and DW (Fig. 2c). The measured DW velocity reaches an order of magnitude greater than the speed of longitudinal sound waves in cuprates^{59,60}, but about four times smaller than the large magnon group velocity of $\text{Sr}_2\text{Cu}_3\text{O}_4\text{Cl}_2$ (see Methods), which sets the upper limit for DW velocity. Notably, the velocity exceeds reports of coherent-magnon-driven DW velocities ($\leq 1 \text{ km s}^{-1}$) in ferromagnetic films^{29,30}.

To understand the microscopic mechanisms behind the DW motion, we performed one-dimensional numerical simulations based on the established mean-field magnetic energy of $\text{Sr}_2\text{Cu}_3\text{O}_4\text{Cl}_2$ ^{49,61,62}, which captures the most essential features of the observed DW motion. In this simplified picture, the DW profile is described by a single variable, the in-plane angle $\phi = \phi(x, t)$, which satisfies (see “Methods”):

$$\partial_t^2 \phi - v_m^2 \partial_x^2 \phi - \frac{v_m^2}{2\lambda^2} \sin 2\phi + \frac{\alpha v_m}{a} \partial_t \phi + \frac{U}{2\lambda^2} \text{sech}^2 \frac{x}{\lambda} (\phi - \phi_c) = 0 \quad (1)$$

where v_m is the magnon velocity, α is the Gilbert damping, and a is the lattice constant. The last term accounts for the DW trapping potential from DW tension and photothermal heat gradients, where U is a phenomenological constant and ϕ_c is the value of ϕ at the DW center. The spin wave excitation is modeled by setting the initial in-plane spin velocities $\dot{\phi}(x, t=0)$ over a Gaussian spatial profile with a sign dependent on the helicity. Solving the effective dynamical equation for realistic material parameters and initial conditions, we were able to reproduce the key experimental features including the helicity dependence, winding number dependence, micron-scale net displacement, fast motion, and slow recovery to equilibrium as shown in Fig. 4c and d (see also Supplementary Section 6, Supplementary Video 3). Our theory and simulations show that the spatial profile of the pump beam is not critical to the observed DW motion. Even under spatially uniform driving, the intrinsic inhomogeneity of the DW itself generates a non-uniform angular acceleration of the spins that propels the DW (Supplementary Section 7). Because our simulation is limited to one dimension, we are unable to capture the transverse motion along the DW line. The observed dynamics are further complicated by the fact that the DW is three-dimensional membrane that extends into the sample bulk, and optical driving is strongest near the surface. In contrast to prior theoretical works on magnon-driven AFM DWs that have focused on easy-axis antiferromagnets^{6,18,19,21,22}, our findings indicate that spin waves can also drive fast DW motion in easy-plane antiferromagnets. Our proposed driving mechanism is unique in that it requires the spin waves to be coherent, with the fast motion in $\text{Sr}_2\text{Cu}_3\text{O}_4\text{Cl}_2$ assisted by the large-angle character of the spin wave excitations.

In conclusion, we established light-induced coherent in-plane AFM spin waves as an effective mechanism for driving fast directional DW motion, which should be applicable to other magnets with easy-plane anisotropy. Optimizing the driving protocol with different pump energies may enable even higher AFM DW velocities and the study of relativistic effects^{19,33,34,63–66}. Furthermore, our results provide an unprecedentedly clear and rich view of DW dynamics that can be used to further refine theoretical calculations beyond simple one-

dimensional models⁶⁷. We anticipate that our findings will stimulate further exploration of how different types of coherent AFM spin waves interact with spin textures in antiferromagnets more broadly.

Methods

Sample growth

$\text{Sr}_2\text{Cu}_3\text{O}_4\text{Cl}_2$ crystals were grown by an optimized method of slow cooling from the melt⁶⁸. Quantities of SrO , SrCl_2 , and CuO powders were mixed in a 1:1:3 stoichiometric ratio and placed in a large high form alumina crucible. The mix was gradually heated in air $1030 \text{ }^\circ\text{C}$, dwelled for 5 h, then cooled to $900 \text{ }^\circ\text{C}$ at a rate of $2 \text{ }^\circ\text{C h}^{-1}$. Placing the crucible in a slight temperature gradient (off-center of the hot chamber of the box furnace) resulted in a cm-sized plate-like single crystal. The samples showed excellent stability in air. X-ray diffraction, Laue X-ray, and low-temperature magnetization measurements were used to verify high sample quality. The samples were affixed to an oxygen-free high-thermal-conductivity copper mount using a small amount of silver epoxy and then cleaved before measurement to leave clean surfaces parallel to the Cu_3O_4 (001) planes.

SHG measurements

SHG rotational anisotropy. SHG rotational anisotropy measurements were carried out using a fast-rotating scattering plane based technique⁶⁹ with laser pulses delivered by a Ti:sapphire amplifier (800 nm fundamental wavelength, 100 fs pulse duration, 100 kHz repetition rate). The beam diameter was $40 \text{ } \mu\text{m}$ with a fluence of 3 mJ/cm^2 .

SHG imaging. Wide-field SHG imaging was performed using the same laser source as that used for rotational anisotropy measurements. The imaging was performed under normal incidence, with linearly polarized excitation, a fluence of 2.3 mJ/cm^2 , and a full-width-at-half-maximum beam diameter of $210 \text{ } \mu\text{m}$, corresponding to 80 mW of average power. The reflected SHG was collected by an achromatic doublet objective lens and imaged onto a cooled charge-coupled device camera. Using the form of DW profile given in Eq. (5), the resulting SHG intensity profile is $I(x) = I_0 [\text{sech}((x - x_0)/\lambda)]^2$, where I_0 is the maximum SHG at the DW center and x_0 is the DW center. This equation was used to extract the DW parameters from the experiments.

Time-resolved SHG imaging. Experiments were performed by splitting off 800 nm light from the same laser source to produce the pump beam. The pump beam was sent through a delay line before reaching the objective doublet lens spatially offset from the principal axis, after which it was focused onto the sample at a 10° angle of incidence. The pump beam spot on the sample was elliptically shaped with a full-width-at-half-maximum of $15 \text{ } \mu\text{m}$ and $10 \text{ } \mu\text{m}$ for the major and minor axes of the ellipse respectively. The reflected pump beam was physically blocked to reduce the amount of scattered pump SHG light that reached the camera. A small amount of SHG light generated by the pump is detected by the camera, which allows us to locate the pump beam relative to the DW. The pump and probe fluences were 8 mJ/cm^2 and 2.3 mJ/cm^2 respectively. The time-resolved two-dimensional DW dynamics (Fig. 2d) were quantitatively extracted by fitting to vertical line cuts of the DW images in Fig. 2c. The fit uncertainties are given as 1 standard error. The location of maximum DW motion ($x = 0$ in Fig. 2d) was used for the one-dimensional dynamics reported in Fig. 2e and Fig. 4). The time-resolved SHG intensity traces in Fig. 3c and d were acquired from time-resolved SHG images on a single-domain region. The SHG intensities were calculated from the average intensity in an approximately $6 \text{ } \mu\text{m}$ by $6 \text{ } \mu\text{m}$ box at the center of the pump excitation profile.

AFM DW dynamics theory and simulation

To characterize the most essential DW dynamics observed in $\text{Sr}_2\text{Cu}_3\text{O}_4\text{Cl}_2$, we adopt a simplified effective 1D model by ignoring the

transverse motion along the DW line, using a normalized Néel vector $\mathbf{n}(x, t)$ to describe the longitudinal DW motion (along x). Based on prior investigations^{34,49,61,62,70,71}, we construct a phenomenological free energy in the continuum as

$$E = S^2 \int dx \left[\eta \mathbf{m}^2 + \beta (\partial_x \mathbf{n})^2 + J_1 \mathbf{m} \cdot \partial_x \mathbf{n} + (J_{pd} \mathbf{M}_F \sigma_1 \mathbf{n} - J_{av} \mathbf{m} \cdot \mathbf{M}_F + K_{\perp} n_z^2) / a \right], \quad (2)$$

where S is the spin quantum number of Cu_I atoms, \mathbf{m} and \mathbf{M}_F are the dimensionless vectors of the local magnetization arising from the Cu_I and Cu_{II} sublattices, respectively. $\eta = J/a$ and $\beta = J_1 a/2$ are the homogeneous and inhomogeneous stiffness constants where a is the lattice constant and $J_1 > 0$ is the nearest-neighbor Heisenberg exchange coupling (illustrated in Fig. 1a). Besides a dominant hard-axis anisotropy $K_{\perp} > 0$ suppressing the out-of-plane canting of \mathbf{n} , we also include $J_{av} > 0$ and $J_{pd} > 0$ as the isotropic and anisotropic pseudo-dipolar interactions affecting the in-plane components, where σ_1 is the Pauli matrix acting on the x - y coordinates. Here we use σ_1 instead of σ_3 (which appears in previous studies) because our convention sets the domains as $\phi \sim \pm \pi/2$ rather than $\pi/4$ and $3\pi/4$. In real materials, there could exist additional anisotropy mechanisms renormalizing J_{pd} , but that will not change the formalism or the phenomenology.

When K_{\perp} dominates other anisotropies, the dynamics of \mathbf{m} , \mathbf{n} and \mathbf{M}_F mainly involves their in-plane components, thus to a good approximation we can parameterize \mathbf{n} by a single variable ϕ such that $\mathbf{n} \approx \cos \phi \hat{x} + \sin \phi \hat{y}$. The in-plane dynamics of \mathbf{n} is inherently related to the low-frequency (acoustic) mode of magnons⁵⁷, for which \mathbf{M}_F is able to adiabatically follow the instantaneous motion of \mathbf{n} . In this regard, \mathbf{M}_F will be essentially locked orthogonally to \mathbf{n} . Since \mathbf{m} is also almost in-plane and $\mathbf{m} \perp \mathbf{n}$ by definition, \mathbf{M}_F is collinear with \mathbf{m} at all locations, ergo $J_{av} \mathbf{m} \cdot \mathbf{M}_F$ reduces to a constant and can be ignored. The same approximation renders the term $J_{pd} \mathbf{M}_F \sigma_1 \mathbf{n}$ proportional to $\cos 2\phi$, serving as an effective in-plane easy-axis anisotropy. Correspondingly, the free energy E becomes a functional of $\phi(x)$.

Such a quasi-1D AFM texture can be described by the action $S[\phi] = S_W[\phi, \partial_t \phi] + \int dt E[\phi, \partial_x \phi]$ where S_W is the Wess-Zumino-Witten term⁷². By integrating out \mathbf{m} using the path integral approach, we obtain the effective action as a functional of ϕ as

$$S_{\text{eff}}[\phi] = \int dt dx \mathcal{L}_{\text{eff}} = S^2 \int dt dx \left[\frac{\hbar^2}{J_1 a S^2} (\partial_t \phi)^2 - \frac{J_1 a}{4} (\partial_x \phi)^2 - \frac{J_{pd} M_F}{a} \cos 2\phi \right], \quad (3)$$

where \hbar is the reduced Planck constant. The Berry phase terms of \mathbf{n} and \mathbf{M}_F have been discarded as we are focusing on the local and in-plane dynamics of $\mathbf{n}(x, t)$. By applying the Euler-Lagrange equation of \mathcal{L}_{eff} in the presence of Rayleigh's dissipation (density) function $\mathcal{R} = \alpha S / (2a) (\partial_t \phi)^2$ ⁷³ to account for the Gilbert damping α , we obtain

$$\partial_t^2 \phi - v_m^2 \partial_x^2 \phi - \frac{v_m^2}{2\lambda^2} \sin 2\phi + \frac{\alpha v_m}{a} \partial_t \phi = 0, \quad (4)$$

where $v_m = J_1 a S / (2\hbar)$ is the magnon velocity and $\lambda = a \sqrt{J_1 / (8J_{pd} M_F)}$ is the DW width parameter. Under the asymptotic boundary conditions $\phi(\pm \infty)$, the static solution to Eq. (4) is obtained as

$$\phi_0(x) = 2 \arctan e^{\pm x/\lambda} \pm \frac{\pi}{2}, \quad (5)$$

where the $+$ ($-$) sign corresponds to the $w = -1/2$ ($+1/2$) DW illustrated in Fig. 3a.

Equation (4) is insufficient to capture the backward DW motion following its initial outward drive, which calls for a trapping potential

to provide an effective restoring force. The physical origin of such a trapping potential could be the surface tension of the DW line and the photo-thermal heating from the laser. To phenomenologically construct a trapping potential, we consider a small virtual displacement of the DW center Δx so that the static profile $\phi_0(x)$ becomes $\phi_0(x - \Delta x)$. Correspondingly, the local change of ϕ is proportional to $\partial_x \phi_0$ (i.e., $\phi'_0(x)$), thus a harmonic trapping potential should be proportional to $\phi_0'^2$. However, $\phi_0'^2$ alone cannot affect the field dynamics because it contributes a constant to the free energy. The potential should be locally proportional to $(\phi - \phi_c)^2$ with ϕ_c the value of ϕ at the DW center, reminiscent of the Klein-Gordon theory. In Fig. 3a, we have $\phi_c = 0$ (π) for the $w = +1/2$ ($-1/2$) DW. Therefore, the trapping potential assumes the form $U \phi_0'^2 (\phi - \phi_c)^2$ where U is a phenomenological constant.

After incorporating the trapping potential into the free energy, we can rederive Eq. (4) as

$$\partial_t^2 \phi - v_m^2 \partial_x^2 \phi - \frac{v_m^2}{2\lambda^2} \sin 2\phi + \alpha' \partial_t \phi + \frac{U}{2\lambda^2} \text{sech}^2 \frac{x}{\lambda} (\phi - \phi_c) = 0, \quad (6)$$

where $\alpha' = \alpha v_m / a$. To solve Eq. (6), we need two initial conditions, $\phi(x, 0)$ and $\dot{\phi}(x, 0)$. Since the laser pulse duration is much shorter than the characteristic time of the Néel vector dynamics, it is natural to set $\phi(x, 0)$ as $\phi_0(x)$ obtained in Eq. (5) while $\dot{\phi}(x, 0)$ (the initial angular velocity of \mathbf{n}) essentially follows the spatial profile of the laser pump. For a normally incident laser carrying a perpendicular spin polarization, $\dot{\phi}(x, 0)$ is proportional to the amount of injected spins by the pump and its sign is determined by the pump helicity because at the $t = 0$ instant (right after the pump is off), $\mathbf{m} \sim \mathbf{n} \times \dot{\mathbf{n}}$ ⁵⁷. With these considerations, we can set

$$\phi(x, 0) = \phi_0(x), \quad (7a)$$

$$\dot{\phi}(x, 0) = \pm \omega_0 \exp[-2(x - x_0)^2 / r_0^2], \quad (7b)$$

where \pm corresponds to opposite helicities, x_0 marks the distance of the pump center from the origin, and r_0 is the radius of the Gaussian beam.

We numerically solved Eq. (6) using the forward Euler method. The parameters used in generating Fig. 4c and d are: $v_m = 0.2 \mu\text{m ps}^{-1}$, $\lambda = 2.86 \mu\text{m}$, $\alpha' = 3.58 \times 10^{-2} \text{ps}^{-1}$, $U = 1.5 \times 10^{-3} \mu\text{m}^2 / \text{ps}^2$, and $\omega_0 = 0.3 \text{ps}^{-1}$.

Data availability

The data that support the findings in this study are available in the main text and the supplementary information. Source data are provided with this paper.

References

- Hinzke, D. & Nowak, U. Domain wall motion by the magnonic spin Seebeck effect. *Phys. Rev. Lett.* **107**, 027205 (2011).
- Kovalev, A. A. & Tserkovnyak, Y. Thermomagnonic spin transfer and Peltier effects in insulating magnets. *Europhys. Lett.* **97**, 67002 (2012).
- Schlickeiser, F., Ritzmann, U., Hinzke, D. & Nowak, U. Role of entropy in domain wall motion in thermal gradients. *Phys. Rev. Lett.* **113**, 097201 (2014).
- Wang, X. S. & Wang, X. R. Thermodynamic theory for thermal-gradient-driven domain-wall motion. *Phys. Rev. B* **90**, 014414 (2014).
- Yan, P., Cao, Y. & Sinova, J. Thermodynamic magnon recoil for domain wall motion. *Phys. Rev. B* **92**, 100408 (2015).

6. Selzer, S., Atxitia, U., Ritzmann, U., Hinzke, D. & Nowak, U. Inertia-free thermally driven domain-wall motion in antiferromagnets. *Phys. Rev. Lett.* **117**, 107201 (2016).
7. Donges, A. et al. Unveiling domain wall dynamics of ferrimagnets in thermal magnon currents: competition of angular momentum transfer and entropic torque. *Phys. Rev. Res.* **2**, 013293 (2020).
8. Ashkin, A. & Dziedzic, J. Interaction of laser light with magnetic domains. *Appl. Phys. Lett.* **21**, 253 (1972).
9. Jiang, W. et al. Direct imaging of thermally driven domain wall motion in magnetic insulators. *Phys. Rev. Lett.* **110**, 177202 (2013).
10. Tetienne, J.-P., et al. Nanoscale imaging and control of domain-wall hopping with a nitrogen-vacancy center microscope. *Science* **344**, 1366 (2014).
11. Ramsay, A. J. et al. Optical spin-transfer-torque-driven domain-wall motion in a ferromagnetic semiconductor. *Phys. Rev. Lett.* **114**, 067202 (2015).
12. Quessab, Y. et al. Helicity-dependent all-optical domain wall motion in ferromagnetic thin films. *Phys. Rev. B* **97**, 054419 (2018).
13. Shokr, Y. A. et al. Steering of magnetic domain walls by single ultrashort laser pulses. *Phys. Rev. B* **99**, 214404 (2019).
14. Hedrich, N. et al. Nanoscale mechanics of antiferromagnetic domain walls. *Nat. Phys.* **17**, 574 (2021).
15. Mikhailov, A. V. & Yaremchuk, A. I. Forced motion of a domain wall in the field of a spin wave. *Sov. J. Exp. Theor. Phys. Lett.* **39**, 354 (1984).
16. Han, D.-S. et al. Magnetic domain-wall motion by propagating spin waves. *Appl. Phys. Lett.* **94**, 112502 (2009).
17. Yan, P., Wang, X. S. & Wang, X. R. All-magnonic spin-transfer torque and domain wall propagation. *Phys. Rev. Lett.* **107**, 177207 (2011).
18. Tveten, E. G., Qaiumzadeh, A. & Brataas, A. Antiferromagnetic domain wall motion induced by spin waves. *Phys. Rev. Lett.* **112**, 147204 (2014).
19. Kim, S. K., Tserkovnyak, Y. & Tchernyshyov, O. Propulsion of a domain wall in an antiferromagnet by magnons. *Phys. Rev. B* **90**, 104406 (2014).
20. Wang, W. et al. Magnon-driven domain-wall motion with the Dzyaloshinskii-Moriya interaction. *Phys. Rev. Lett.* **114**, 087203 (2015).
21. Qaiumzadeh, A., Kristiansen, L. A. & Brataas, A. Controlling chiral domain walls in antiferromagnets using spin-wave helicity. *Phys. Rev. B* **97**, 020402 (2018).
22. Yu, W., Lan, J. & Xiao, J. Polarization-selective spin wave driven domain-wall motion in antiferromagnets. *Phys. Rev. B* **98**, 144422 (2018).
23. Oh, S.-H., Kim, S. K., Xiao, J. & Lee, K.-J. Bidirectional spin-wave-driven domain wall motion in ferrimagnets. *Phys. Rev. B* **100**, 174403 (2019).
24. Rodrigues, D., Salimath, A., Everschor-Sitte, K. & Hals, K. Spin-wave driven bidirectional domain wall motion in kagome antiferromagnets. *Phys. Rev. Lett.* **127**, 157203 (2021).
25. Lan, J. & Xiao, J. Spin wave driven domain wall motion in easy-plane ferromagnets: a particle perspective. *Phys. Rev. B* **106**, L020404 (2022).
26. Jiao, X., Wang, X. S. & Lan, J. Universal spin wave driven domain wall velocity in biaxial ferromagnets. *Phys. Rev. B* **109**, 094428 (2024).
27. Woo, S., Delaney, T. & Beach, G. S. D. Magnetic domain wall depinning assisted by spin wave bursts. *Nat. Phys.* **13**, 448 (2017).
28. Ogawa, N. et al. Photodrive of magnetic bubbles via magnetoelastic waves. *Proc. Natl Acad. Sci. USA* **112**, 8977 (2015).
29. Han, J., Zhang, P., Hou, J. T., Siddiqui, S. A., and Liu, L., Mutual control of coherent spin waves and magnetic domain walls in a magnonic device. *Science* **366**, 1121 (2019).
30. Fan, Y. et al. Coherent magnon-induced domain-wall motion in a magnetic insulator channel. *Nat. Nanotechnol.* **18**, 1000 (2023).
31. Gomonay, O., Baltz, V., Brataas, A. & Tserkovnyak, Y. Antiferromagnetic spin textures and dynamics. *Nat. Phys.* **14**, 213 (2018).
32. Han, J., Cheng, R., Liu, L., Ohno, H. & Fukami, S. Coherent antiferromagnetic spintronics. *Nat. Mater.* **22**, 684 (2023).
33. Gomonay, O., Jungwirth, T. & Sinova, J. High antiferromagnetic domain wall velocity induced by Néel spin-orbit torques. *Phys. Rev. Lett.* **117**, 017202 (2016).
34. Shiino, T. et al. Antiferromagnetic domain wall motion driven by spin-orbit torques. *Phys. Rev. Lett.* **117**, 087203 (2016).
35. Yu, H., Xiao, J. & Schultheiss, H. Magnetic texture based magnonics. *Phys. Rep.* **905**, 1 (2021).
36. Kimel, A. V. et al. Ultrafast non-thermal control of magnetization by instantaneous photomagnetic pulses. *Nature* **435**, 655 (2005).
37. Satoh, T. et al. Spin oscillations in antiferromagnetic NiO triggered by circularly polarized light. *Phys. Rev. Lett.* **105**, 077402 (2010).
38. Satoh, T., et al. Directional control of spin-wave emission by spatially shaped light. *Nat. Photon.* **6**, 662 (2012).
39. Satoh, T., Iida, R., Higuchi, T., Fiebig, M. & Shimura, T. Writing and reading of an arbitrary optical polarization state in an antiferromagnet. *Nat. Photon.* **9**, 25 (2015).
40. Tzschaschel, C. et al. Ultrafast optical excitation of coherent magnons in antiferromagnetic NiO. *Phys. Rev. B* **95**, 174407 (2017).
41. Kimel, A. V. et al. Optical excitation of antiferromagnetic resonance in TmFeO₃. *Phys. Rev. B* **74**, 060403 (2006).
42. Kampfrath, T. et al. Coherent terahertz control of antiferromagnetic spin waves. *Nat. Photon.* **5**, 31 (2011).
43. Hortensiusset, J. R., al. Coherent spin-wave transport in an antiferromagnet. *Nat. Phys.* **17**, 1001 (2021).
44. Cheong, S.-W., Fiebig, M., Wu, W., Chapon, L. & Kiryukhin, V. Seeing is believing: visualization of antiferromagnetic domains. *npj Quantum Mater.* **5**, 1 (2020).
45. Zayko, S. et al. Ultrafast high-harmonic nanoscopy of magnetization dynamics. *Nat. Commun.* **12**, 6337 (2021).
46. Jangid, R. et al. Extreme domain wall speeds under ultrafast optical excitation. *Phys. Rev. Lett.* **131**, 256702 (2023).
47. Stupakiewicz, A., Maziewski, A., Davidenko, I. & Zablotskii, V. Light-induced magnetic anisotropy in Co-doped garnet films. *Phys. Rev. B* **64**, 064405 (2001).
48. Kirilyuk, A., Kimel, A. V. & Rasing, T. Ultrafast optical manipulation of magnetic order. *Rev. Mod. Phys.* **82**, 2731 (2010).
49. Chou, F. C. et al. Ferromagnetic moment and spin rotation transitions in tetragonal antiferromagnetic Sr₂Cu₃O₄Cl₂. *Phys. Rev. Lett.* **78**, 535 (1997).
50. Seyler, K. L. et al. Direct visualization and control of antiferromagnetic domains and spin reorientation in a parent cuprate. *Phys. Rev. B* **106**, L140403 (2022).
51. Fiebig, M., Fröhlich, D., Lottermoser, T. & Maat, M. Probing of ferroelectric surface and bulk domains in RMnO₃ (R=Y, R=Ho) by second harmonic generation. *Phys. Rev. B* **66**, 144102 (2002).
52. Schmitt, C. et al. Identifying the domain-wall spin structure in antiferromagnetic NiO/Pt. *Phys. Rev. B* **107**, 184417 (2023).
53. Wörnle, M. S. et al. Coexistence of Bloch and Néel walls in a collinear antiferromagnet. *Phys. Rev. B* **103**, 094426 (2021).
54. Parks, B. et al. Magnetization measurements of antiferromagnetic domains in Sr₂Cu₃O₄Cl₂. *Phys. Rev. B* **63**, 134433 (2001).
55. Shan, J.-Y. et al. Dynamic magnetic phase transition induced by parametric magnon pumping. *Phys. Rev. B* **109**, 054302 (2024).
56. Hansteen, F., Kimel, A., Kirilyuk, A. & Rasing, T. Nonthermal ultrafast optical control of the magnetization in garnet films. *Phys. Rev. B* **73**, 014421 (2006).
57. Cheng, R., Daniels, M. W., Zhu, J.-G. & Xiao, D. Ultrafast switching of antiferromagnets via spin-transfer torque. *Phys. Rev. B* **91**, 064423 (2015).
58. Katsumata, K. et al. Direct observation of the quantum energy gap in S = ½ tetragonal cuprate antiferromagnets. *Europhys. Lett.* **54**, 508 (2001).

59. Migliori, A. et al. Elastic constants and specific-heat measurements on single crystals of La_2CuO_4 . *Phys. Rev. B* **41**, 2098 (1990).
 60. Abd-Shukor, R. Ultrasonic and elastic properties of Tl- and Hg-based cuprate superconductors: A review. *Phase Trans.* **91**, 48 (2018).
 61. Kim, Y. J. et al. Neutron scattering study of $\text{Sr}_2\text{Cu}_3\text{O}_4\text{Cl}_2$. *Phys. Rev. B* **64**, 024435 (2001).
 62. Gomonay, H. V., Korniienko, I. G. & Loktev, V. M. Theory of magnetization in multiferroics: Competition between ferromagnetic and antiferromagnetic domains. *Phys. Rev. B* **83**, 054424 (2011).
 63. Haldane, F. D. M. Nonlinear field theory of large-spin Heisenberg antiferromagnets: Semiclassically quantized solitons of the one-dimensional easy-axis Néel state. *Phys. Rev. Lett.* **50**, 1153 (1983).
 64. Bar'yakhtar, I. V. and I. B. A. Dynamic solitons in a uniaxial antiferromagnet. *Sov. Phys. JETP* **58**, 190 (1984).
 65. Yuan, H. Y., Wang, W., Yung, M.-H. & Wang, X. R. Classification of magnetic forces acting on an antiferromagnetic domain wall. *Phys. Rev. B* **97**, 214434 (2018).
 66. Caretta, L. & Avci, C. O. Domain walls speed up in insulating ferromagnetic garnets. *APL Mater.* **12**, 011106 (2024).
 67. Cheng, R. et al. Magnetic domain wall skyrmions. *Phys. Rev. B* **99**, 184412 (2019).
 68. Noro, S. et al. Magnetic properties of $\text{Ba}_2\text{Cu}_3\text{O}_4\text{Cl}_2$ single crystals. *Mater. Sci. Eng.: B* **25**, 167 (1994).
 69. Harter, J. W., Niu, L., Woss, A. J. & Hsieh, D. High-speed measurement of rotational anisotropy nonlinear optical harmonic generation using position-sensitive detection. *Opt. Lett.* **40**, 4671 (2015).
 70. Kastner, M. A. et al. Field-dependent antiferromagnetism and ferromagnetism of the two copper sublattices in $\text{Sr}_2\text{Cu}_3\text{O}_4\text{Cl}_2$. *Phys. Rev. B* **59**, 14702 (1999).
 71. Tveten, E. G., Müller, T., Linder, J. & Brataas, A. Intrinsic magnetization of antiferromagnetic textures. *Phys. Rev. B* **93**, 104408 (2016).
 72. Fradkin, E., et al. *Field theories of condensed matter physics* (Cambridge University Press, 2013).
 73. Kamra, A., Troncoso, R. E., Belzig, W. & Brataas, A. Gilbert damping phenomenology for two-sublattice magnets. *Phys. Rev. B* **98**, 184402 (2018).
- SLAC (crystal growth and sample characterization) was supported by the U.S. Department of Energy (DOE), Office of Science, Basic Energy Sciences, Materials Sciences and Engineering Division, under contract DE-AC02-76SF00515.

Author contributions

K.L.S. and D.H. conceived the experiment. K.L.S. and D.V.B. performed the experiments. K.L.S. analyzed data. H.Z. and R.C. led theoretical modeling and interpretation. C.R.R. and Y.S.L. synthesized and characterized samples. K.L.S. and D.H. wrote the paper with input from all authors.

Competing interests

The authors declare no competing interests.

Additional information

Supplementary information The online version contains supplementary material available at <https://doi.org/10.1038/s41467-025-64803-2>.

Correspondence and requests for materials should be addressed to David Hsieh.

Peer review information *Nature Communications* thanks Mikhail Katsnelson and the other anonymous reviewer(s) for their contribution to the peer review of this work. A peer review file is available.

Reprints and permissions information is available at <http://www.nature.com/reprints>

Publisher's note Springer Nature remains neutral with regard to jurisdictional claims in published maps and institutional affiliations.

Open Access This article is licensed under a Creative Commons Attribution-NonCommercial-NoDerivatives 4.0 International License, which permits any non-commercial use, sharing, distribution and reproduction in any medium or format, as long as you give appropriate credit to the original author(s) and the source, provide a link to the Creative Commons licence, and indicate if you modified the licensed material. You do not have permission under this licence to share adapted material derived from this article or parts of it. The images or other third party material in this article are included in the article's Creative Commons licence, unless indicated otherwise in a credit line to the material. If material is not included in the article's Creative Commons licence and your intended use is not permitted by statutory regulation or exceeds the permitted use, you will need to obtain permission directly from the copyright holder. To view a copy of this licence, visit <http://creativecommons.org/licenses/by-nc-nd/4.0/>.

© The Author(s) 2025

Acknowledgements

We acknowledge helpful conversations with Jonathan Curtis and Eugene Demler. D.H. acknowledges support for time-resolved SHG measurements from a Brown Investigator Award, a program of the Brown Institute for Basic Sciences at the California Institute of Technology, as well as the Institute for Quantum Information and Matter (IQIM), an NSF Physics Frontiers Center (PHY-2317110). D.H. acknowledges support for instrumentation from the David and Lucile Packard Foundation. K.L.S. acknowledges a Caltech Prize Postdoctoral Fellowship. R.C. and H.Z. were supported by the Air Force Office of Scientific Research under Grant No. FA9550-19-1-0307. The work at Stanford and